Interrater and intrarater reliability of aqueduct CSF flow parameters measured by phase-contrast MRI in healthy adults

Pan Liu, Yann Attekeble, Jiachen Xie, Kimi Owashi, Heimiri Monnier, Serge Metanbou, Cyrille Capel, Olivier Balédent

Original Article

Interrater and intrarater reliability of aqueduct CSF flow parameters measured by phase-contrast MRI in healthy adults

Pan Liu[1,2#^], Yann Attekeble[3#], Jiachen Xie[4#], Kimi Owashi[1,2], Heimiri Monnier[2], Serge Metanbou[5], Cyrille Capel[2,6], Olivier Balédent[1,2^]

[1]Medical Image Processing Department, CHU Amiens-Picardy University Hospital, Amiens, France; [2]CHIMERE UR 7516, Jules Verne University of Picardy, Amiens, France; [3]University of Lille, Lille, France; [4]Oncology Department, CHU Amiens-Picardy University hospital, Amiens, France; [5]Radiology Department, CHU Amiens-Picardy University hospital, Amiens, France; [6]Neurosurgery Department, CHU Amiens-Picardy University hospital, Amiens, France

Contributions: (I) Conception and design: P Liu, Y Attekeble, J Xie, O Balédent; (II) Administrative support: O Balédent, C Capel; (III) Provision of study materials or patients: O Balédent, C Capel, H Monnier, S Metanbou, K Owashi; (IV) Collection and assembly of data: P Liu, Y Attekeble, J Xie, H Monnier; (V) Data analysis and interpretation: P Liu, Y Attekeble, J Xie; (VI) Manuscript writing: All authors; (VII) Final approval of manuscript: All authors.

[#]These authors contributed equally to this work.

Correspondence to: Pan Liu, PhD; Olivier Balédent, PhD. Medical Image Processing Department, CHU Amiens-Picardy University Hospital, 1 Rue du Professeur Christian Cabrol, Amiens, 80000, France; CHIMERE UR 7516, Jules Verne University of Picardy, Amiens, 80000, France. Email: Liu.Pan@chu-amiens.fr; Olivier.Baledent@chu-amiens.fr.

Background: Cerebrospinal fluid (CSF) hydrodynamic parameters at the aqueduct of Sylvius are critical for understanding and diagnosing neurodegenerative diseases. This study aims to assess both interrater and intrarater reliability of aqueduct CSF flow parameters measured by phase-contrast magnetic resonance imaging (PC-MRI) across different operators in healthy adults.

Methods: Thirty-eight healthy adult participants were included in the study. Three operators independently quantified aqueduct CSF flow parameters using PC-MRI. Parameters measured included surface (cross-sectional area of aqueduct), net flow per stroke, flow amplitude, peak mean velocity, and stroke volume. Intraclass correlation coefficients [ICC (3,1) for interrater and ICC (1,1) for intrarater reliability] were used to evaluate measurement consistency. Non-parametric tests assessed the impact of velocity encoding (VENC), sex, age, and cardiac period on measurement variability.

Results: Most aqueduct parameters exhibited good to excellent reliability, with ICC (3,1) values ranging from 0.75 to 0.99. Surface demonstrated poor reliability with an ICC (3,1) of 0.37 and ICC (1,1) of 0.33, 0.54 and 0.84. Net flow rate demonstrated moderate consistency with an ICC (3,1) of 0.84 and ICC (1,1) of 0.78, 0.87 and 0.92. VENC significantly increased noise intensity and decreased net flow rate reliability ($P<0.01$). Gender analysis showed that males had significantly higher surface area ($P<0.01$), stroke volume ($P=0.04$), and net flow rate ($P<0.01$) compared to females.

Conclusions: The study confirmed that most aqueduct CSF flow parameters measured by PC-MRI are reliable both across different operators and in repeated measurements. However, net flow rate and surface area require careful consideration due to lower reliability. These findings provide a valuable reference for the clinical application of CSF hydrodynamic measurements in diagnosing and monitoring neurodegenerative diseases.

^ ORCID: Pan Liu, 0000-0003-0559-6432; Olivier Balédent, 0000-0001-6028-6440.

Keywords: Cerebrospinal fluid hydrodynamics (CSF hydrodynamics); phase-contrast magnetic resonance imaging (PC-MRI); aqueduct of Sylvius; inter-operator reliability; neurodegenerative diseases

Submitted Aug 04, 2024. Accepted for publication Nov 28, 2024. Published online Jun 30, 2025.
doi: 10.21037/qims-24-1589
View this article at: https://dx.doi.org/10.21037/qims-24-1589

Introduction

Cerebrospinal fluid (CSF) plays a crucial role in protecting the brain, removing metabolic waste, and maintaining homeostasis (1-6). Neurodegenerative diseases often exhibit changes in CSF hydrodynamic parameters before morphological abnormalities arise (7-14). A better understanding of CSF hydrodynamics is essential for elucidating the pathogenesis and diagnosis of these conditions.

The hydrodynamics of CSF are highly complex. According to the Monro-Kellie doctrine, the intracranial volume remains constant, with CSF dynamics compensating for changes in blood and brain tissue volumes (15-18). Besides the net flow rate related to production and absorption rates, there are also various frequencies of pulsatile flow driven by cardiac and respiratory cycles, as well as cerebral autoregulation (19-23). The aqueduct of Sylvius is a narrow channel connecting the third and fourth ventricles. CSF oscillates through the aqueduct driven by the pressure differential between the subarachnoid space and the ventricles (24,25). Hydrodynamic parameters of CSF at the aqueduct have been linked to various neurodegenerative diseases and have numerous clinical applications, such as diagnosing normal pressure hydrocephalus (9-12), monitoring shunt function (26), Chiari malformation (8), and assessing aqueduct stenosis (27,28).

Phase-contrast magnetic resonance imaging (PC-MRI) is widely used in clinical practice to observe CSF flow curves over an average cardiac cycle (29). Commonly used aqueduct parameters include net flow per stroke, flow amplitude, peak mean velocity, and stroke volume. However, due to the typically low flow velocities in the aqueduct (often below 10 cm/s) compared to cerebral blood flow, low velocity encoding (VENC) settings are required for imaging, which can increase susceptibility to background noise. Additionally, the small cross-sectional area of the aqueduct necessitates precise segmentation during post-processing. Consequently, whether these parameters demonstrate good clinical reproducibility across different operators is important and remains uncertain.

This study aims to address this gap by quantifying the reliability of aqueduct flow parameters measured by 3 different operators in healthy adults and analysing the impact of various factors such as VENC, sex, age, and cardiac period on measurement variability. By establishing the consistency of these measurements, we can provide a more robust reference for their clinical application in diagnosing and monitoring neurodegenerative diseases. We present this article in accordance with the GRRAS reporting checklist (30) (available at https://qims.amegroups.com/article/view/10.21037/qims-24-1589/rc).

Methods

Study conditions, participants and operators

The prospective study was conducted in accordance with the Declaration of Helsinki and its subsequent amendments. This study was approved by the local Ethics Review Committee (CPP Nord Ouest II, Amiens, France; reference: PI2019_843_0056). Informed consent was obtained from all individual participants involved in the study.

Healthy young adult volunteers were recruited through convenience sampling from the local community. Inclusion criteria required participants to be generally healthy, with no history of neurological, psychiatric, severe general disease, or alcoholism.

Exclusion criteria included any contraindications for MRI, such as metal implants or severe claustrophobia, a history of cerebrovascular or respiratory disease, and any abnormalities detected during a preliminary clinical MRI exam. Each MRI session lasted approximately 30 minutes.

Between February 2020 and November 2023, a total of 40 participants were initially screened. During imaging acquisition, two participants were excluded due to body size limitations that prevented proper positioning within the MRI scanner. Ultimately, 38 participants completed the imaging process without any adverse events (*Figure 1*).

Three fixed operators were responsible for post-processing all participants. Operator 1 has seven years of post-processing experience and possesses basic physiological knowledge. Operator 2 has two months of post-processing

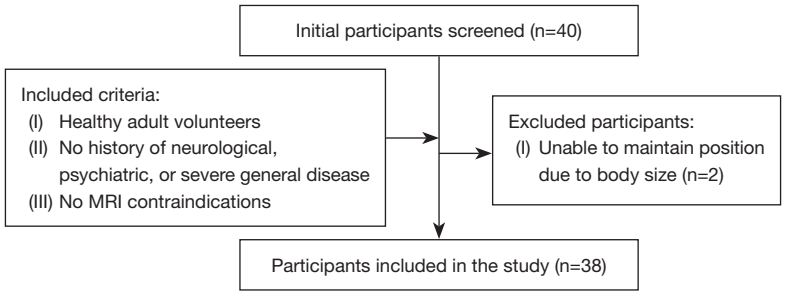

Figure 1 The flowchart of the participants in this study. MRI, magnetic resonance imaging.

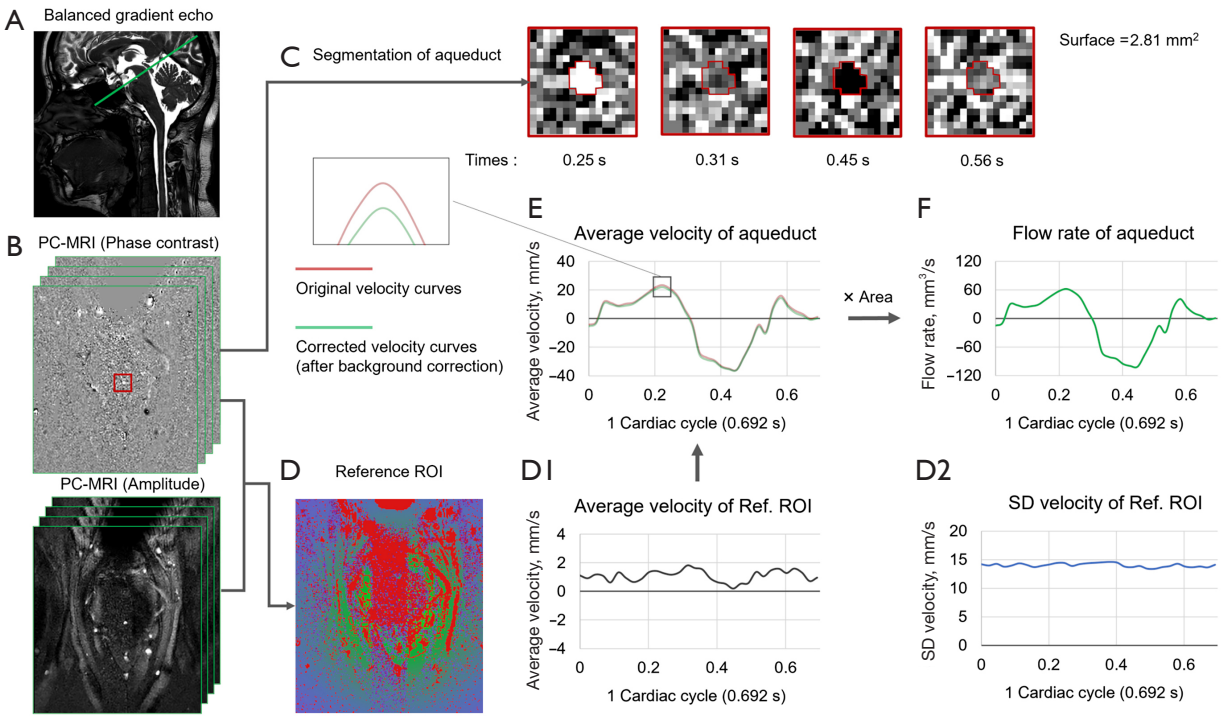

Figure 2 Image acquisition and post-processing workflow. (A) 3D balanced gradient echo image with the green line indicating the PC-MRI slice position. (B) Thirty-two phase-contrast and amplitude images from PC-MRI. (C) Aqueduct ROI within phase contrast images at four cardiac phases. (D) Reference region defined using the fully automatic method (green area), used to extract the average velocity signal (D1) and the velocity standard deviation signal (D2) within the reference ROI. (E) Corrected velocity signal obtained by subtracting the reference velocity signal from the average velocity signal within the aqueduct ROI. (F) Flow signal obtained by multiplying the corrected velocity signal by the surface of the aqueduct. PC-MRI, phase contrast magnetic resonance imaging; ROI, region of interest; SD, standard deviation.

experience. Operator 3 underwent seven days of training and practice. Both operator 2 and operator 3 were validated for accurate use of the post-processing software.

Image acquisition

The acquisition planes, oriented perpendicular to the aqueduct, were localized using a sagittal 3D balanced gradient echo sequence with parameters: TR =5.5 ms, TE =2.2 ms, FOV =180×180 mm^2, spatial resolution =0.6×0.6×1.2 mm^3, and flip angle =45°. This sequence produced a high signal for CSF (*Figure 2A*).

The aqueduct flow was quantified using conventional cardiac-gated phase-contrast MRI (PC-MRI). After

approximately one to two minutes of acquisition, 32 phase-contrast and amplitude images corresponding to cardiac phases were obtained. These images represent the flow variations over an average cardiac cycle (*Figure 2B*).

The parameters were set as follows: FOV =90×90 mm^2, acquisition spatial resolution =0.5×0.5 mm^2, thickness =2 mm, sampling time =56–153 s, flip angle =30°, TR =14.7 ms, TE =7.7 ms, and sensitivity encoding factor =1.5. VENC was set to 10 or 20 cm/s based on individual flow rates to avoid aliasing effects. The direction from the fourth ventricle to the third ventricle was defined as the positive direction.

Image post-processing

Image post-processing was performed using the specialized PC-MRI software Flow-2.0 (31,32), which includes the following steps:

Semi-automatic segmentation based on the velocity frequency characteristics of each pixel in the phase-contrast images, primarily focusing on the cardiac frequency component. The region of interest (ROI) in the aqueduct was fixed. Subsequently, the average velocity within the ROI was calculated for each phase-contrast image to obtain the mean flow velocity curve (*Figure 2C*).

All operators employed the fully automatic background field correction algorithm to eliminate the variability introduced by manual processing. The basic principles of this algorithm are shown in Figure S1. The objective was to select a region of stationary tissue around the aqueduct as reference ROI (*Figure 2D*), and calculate the average velocity within the reference ROI for each phase-contrast image, establishing this as the new zero velocity (*Figure 2D*, 1). The standard deviation of the velocity within the ROI was recorded as the noise value of the velocity images for subsequent comparisons (*Figure 2D*, 2). Subsequently, the flow velocity curve was adjusted by subtracting the reference velocity curve, thereby obtaining the corrected flow velocity curve (*Figure 2E*).

In instances where the maximum flow velocity exceeded the VENC, the software provided the functionality to perform aliasing correction (section 4.6.2 in 32). The final flow rate signal was obtained by multiplying the average flow velocity signal within the aqueduct ROI by its surface area, where surface is calculated as the product of the number of pixels within the ROI and the pixel size, as illustrated in *Figure 2F*.

Signal post-processing and parameter extraction

The following signal parameters were extracted or calculated for subsequent consistency quantification:

The pixel velocity curve represents the velocity curve of the pixel with the maximum flow velocity amplitude within the aqueduct ROI. The pixel velocity maximum indicates the highest flow velocity of pixel velocity curve (*Figure 3A,3B*).

Velocity maximum represents the average velocity at the moment of maximum flow from the fourth ventricle to the third ventricle. Similarly, velocity minimum represents the average velocity at the moment of maximum flow from the third ventricle to the fourth ventricle (*Figure 3C*).

Flow rate maximum and flow rate minimum indicate the maximum flow rates in both directions. Stroke volume positive is the volume of fluid flowing in the positive direction within one cardiac cycle, obtained by integrating the flow rate curve above the x-axis. Conversely, stroke volume negative represents the volume of fluid pumped from the third to the fourth ventricle, obtained by integrating the flow rate curve below the x-axis. Stroke volume is calculated as the mean of the positive and negative stroke volumes. The net flow rate is calculated as the mean of the flow rate curve (*Figure 3D*).

The background field velocity error is represented by the mean of the reference velocity curve (*Figure 3E*). The noise intensity of the reference field (SD-V-Ref.) is indicated by the mean of the standard deviation curve within the reference ROI (*Figure 3F*).

The aforementioned parameters were quantified by each operator. The mean value of the data provided by the three operators was established as the final parameter value for subsequent analysis. Furthermore, the mean percentage error of each operator's data was calculated in relation to the mean, and this was used as a parameter to quantify consistency.

All operators performed a second set of repeated measurements with a minimum interval of one week. These data were ultimately used for interrater reliability analysis and for assessing intrarater reliability in comparison to the initial measurements.

All measurements were conducted independently, with no communication between operators. During the second measurement session, operators had no access to their initial results.

Statistical analysis

Sample size determination was based on a significance level

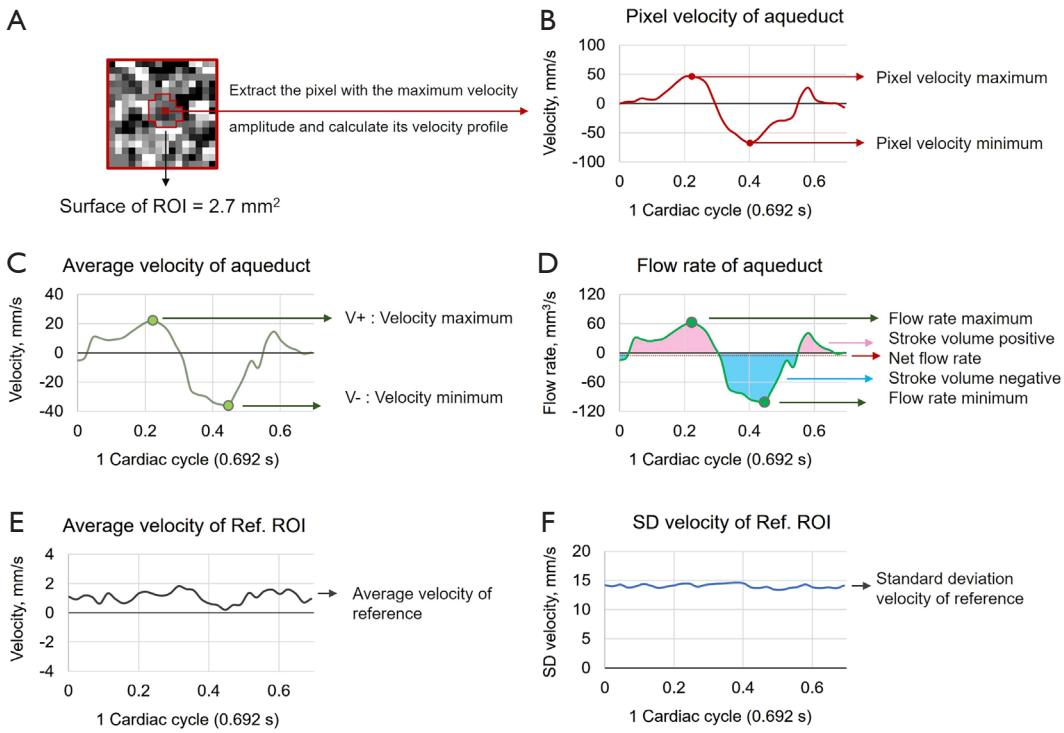

Figure 3 Flow parameter schematic. (A) Aqueduct ROI and pixel with the maximum velocity amplitude. (B) Extraction of velocity extrema corresponding to the pixel with the maximum velocity. (C) Extraction of aqueduct velocity curve extrema, with the direction from the fourth ventricle to the third ventricle defined as positive. (D) Extraction of flow rate extrema from the aqueduct flow rate curve, calculation of stroke volume positive and stroke volume negative by integrating the area under the flow rate curve above and below the x-axis, respectively. Stroke volume is the mean of these values. Net flow rate is calculated as the mean of the flow rate curve. (E) The mean of the reference ROI's average velocity curve represents the reference velocity error, and (F) the mean of the reference ROI's standard deviation curve indicates the background field noise intensity. ROI, region of interest; SD, standard deviation.

(α) of 0.05 and a target power of 0.8. With a sample size of 38, this study was designed to detect a minimum effect size of approximately 0.93. Statistical calculations were performed using SPSS software (version 26.0; IBM Corp., Armonk, NY, USA), and necessary plots were generated using Origin software. The consistency of measurements among the three operators was assessed using the intraclass correlation coefficient (ICC), specifically ICC (3,1), which is a two-way mixed-effects model designed to assess absolute agreement and provides ICC values for single measurements. To quantify the intrarater reliability of each operator's repeated measurements across all parameters, ICC (1,1) was calculated. A one-way random-effects model was used to assess the absolute agreement between two measurement sessions for each operator, with the single measurement values being considered. ICC values were interpreted as follows: values less than 0.5 indicate poor reliability, values between 0.5 and 0.75 indicate moderate reliability, values between 0.75 and 0.9 indicate good reliability, and values greater than 0.9 indicate excellent reliability. In addition, intrarater reliability was further quantified and visualized using Bland-Altman analysis. For each parameter, the mean percentage difference and limits of agreement (LOA) range were recorded for each operator to provide a comprehensive assessment of measurement variability. Data are presented as mean ± SD and illustrated using Q1-Q3 values to provide a comprehensive view of the distribution. The Mann-Whitney *U* test was used to verify differences in medians, and Spearman's rank correlation was employed to assess correlations. Significance was determined with a two-tailed P value <0.05.

Results

Thirty-eight human participants were included in the study [20 men and 18 women; mean ± standard deviation (SD)

Table 1 Distribution of aqueduct flow parameters measured by three operators

Parameters	Op-1	Op-2	Op-3	Mean	Diff%	ICC (3,1)
Surface (mm^2)	2.82±0.70	1.83±0.67	2.66±0.68	2.44±0.58	19.5±9.2	0.37
	[2.39, 3.23]	[1.41, 2.39]	[2.25, 2.95]	[2.02, 2.95]	[12.4, 25.9]	
Stroke volume + (mm^3)	36±21	27±18	33±17	32±18	13.0±7.8	0.89
	[20, 47]	[17, 38]	[20, 44]	[19, 43]	[7.1, 16.1]	
Stroke volume – (mm^3)	42±23	33±18	39±19	38±20	11.2±7.1	0.90
	[25, 49]	[21, 36]	[26, 49]	[25, 46]	[6.0, 16.4]	
Stroke volume (mm^3/CC)	39±22	30±18	36±18	35±19	11.9±7.1	0.90
	[22, 49]	[20, 36]	[24, 48]	[22, 44]	[6.1, 15.8]	
Flow rate maximum (mm^3/s)	139±62	106±54	131±53	125±55	13.2±7.9	0.85
	[91, 170]	[66, 136]	[91, 167]	[81, 157]	[7.3, 18.9]	
Flow rate minimum (mm^3/s)	162±67	123±54	151±58	146±58	11.9±6.7	0.82
	[113, 188]	[81, 163]	[105, 200]	[100, 183]	[7.9, 16.8]	
Net flow rate (mm^3/s)	−10±8	−8±7	−10±8	−9±7	33.3±50.5	0.84
	[−13, −6]	[−12, −3]	[−14, −5]	[−13, −5]	[11.3, 30.7]	
Velocity maximum (mm/s)	49±16	57±20	49±17	52±17	8.1±4.6	0.86
	[38, 63]	[43, 69]	[39, 59]	[40, 63]	[4.9, 10.8]	
Velocity minimum (mm/s)	56±14	68±18	57±19	60±16	9.5±5.7	0.75
	[45, 65]	[55, 82]	[44, 68]	[49, 72]	[5.4, 12.2]	
Pixel velocity maximum (mm/s)	85±29	83±30	82±28	83±28	5.1±7.6	0.90
	[59, 105]	[61, 105]	[59, 105]	[62, 103]	[0.16, 7.1]	
Pixel velocity minimum (mm/s)	96±26	92±29	95±28	94±27	4.4±4.6	0.93
	[78, 116]	[74, 112]	[74, 114]	[76, 110]	[0.1, 8.3]	
Average velocity of Ref. (mm/s)	−1.1±4.2	−1.1±4.2	−1.1±4.2	−1.1±4.2	3.9±9.2	0.99
	[−2.0, 1.4]	[−2.7, 1.4]	[−2.7, 1.4]	[−2.1, 1.4]	[0.7, 3.9]	
Standard deviation of Ref.	19.9±6.9	20.3±7.2	20.3±7.2	20.2±7.0	0.8±3.7	0.96
	[14.3, 25.7]	[14.3, 26.3]	[14.3, 26.2]	[14.3, 26.2]	[0.1, 0.3]	

Op-1 represents measurements from Operator 1. Op-2 denotes Operator 2. Op-3 denotes Operator 3. Data are presented as mean ± standard deviation and [Q1, Q3]. Ref. represent the reference. Diff% represents the average percentage difference of the three operators relative to their mean value. ICC (3,1) indicates the intraclass correlation coefficient using a two-way mixed-effects model for absolute agreement. ICC, intraclass correlation coefficient.

age: 25.3±3.8; age range: 19–35 years]. Data from all thirty-eight participants were successfully acquired and quantified by all three operators. Three participants exhibited correctable aliasing under the condition of VENC =10.

Distribution of aqueduct parameters and interrater reliability

As shown in *Table 1*, the surface area showed moderate consistency with an ICC of 0.37, indicating variability among the operators. All other parameters exhibited good reliability (ICC between 0.75 and 0.9) or excellent reliability (ICC greater than 0.9).

Due to the net flow rate (−9±7 mm^3/s) and average velocity of the reference region (−1.1±4.2 mm/s) being close to zero, their percentage differences were relatively large (33.3%±50.5% and 3.9%±9.2%, respectively). Excluding these two values, the surface area had the

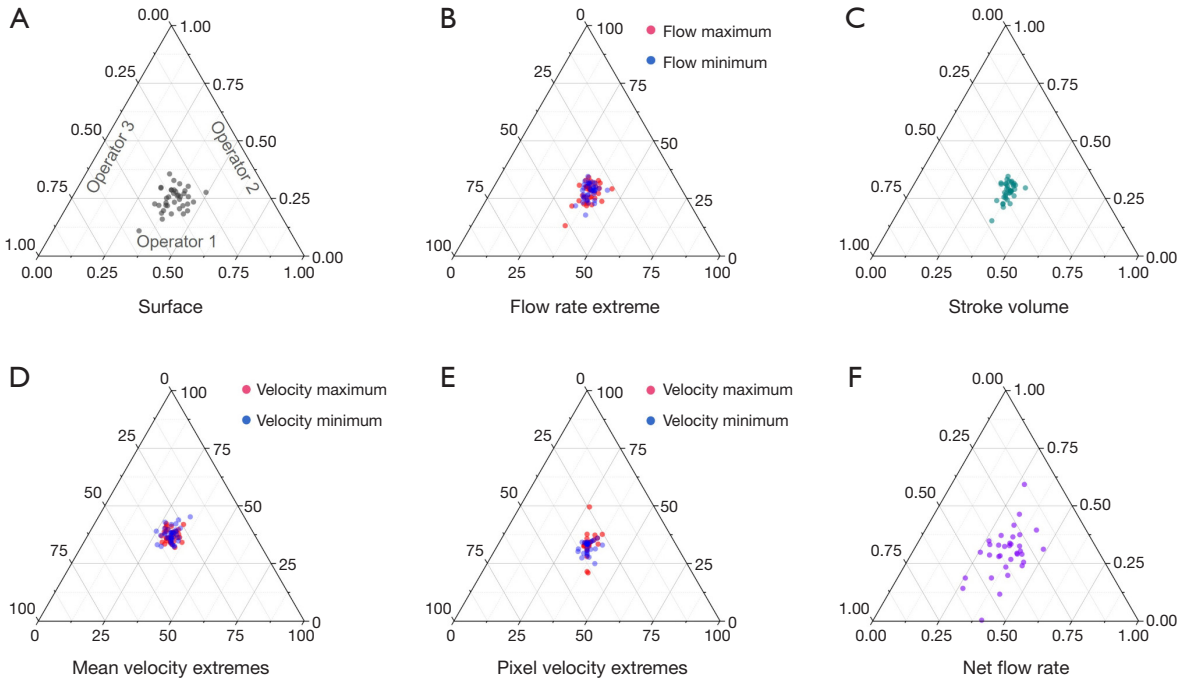

Figure 4 Ternary scatter plots. Showing normalized measurements from all operators (0–1 or 1–100). (A) Surface area measurements. (B) Flow rate measurements: red for positive direction (fourth to third ventricle), blue for negative direction. (C) Stroke volume measurements. (D) Mean velocity extremes measurements: red for positive extremes, blue for negative extremes. (E) Pixel velocity extremes measurements: red for positive extremes, blue for negative extremes. (F) Net flow rate measurements.

largest percentage difference (19.5%±9.2%), while the Pixel velocity maximum (5.1%±7.6%) and Pixel velocity minimum (4.4%±4.6%) had the smaller percentage differences.

Analysis of physiological parameters using the mean values from the three operators revealed that the net flow was significantly less than zero (–9±7 mm^3/s, P<0.001). The stroke volume, flow rate extrema, and flow velocity extrema in the negative direction (from the third ventricle to the fourth ventricle) were significantly greater than those in the positive direction (all P<0.01).

Visualization of interrater reliability of aqueduct parameters

Figure 4 presents ternary scatter plots for several parameters. The three coordinates for each point are obtained by dividing each operator's measured value by the sum of the three operators' values, thus ensuring the sum of the coordinates for each point equals 1 or 100%. Points indicating higher measurement reliability are observed to cluster near (0.33, 0.33, 0.33).

The data indicates that the surface area exhibits a lower degree of reliability in comparison to the flow rate, flow velocity, and stroke volume. It is noteworthy that the net flow parameter exhibits the lowest reliability, with the most dispersed scatter plot distribution.

Figure 5 presents 3D scatter plots for three parameters, with the three axes representing the three operators. The 95% confidence ellipsoid is shown for each parameter. The long axis of the confidence ellipsoid indicates the main direction of parameter distribution, while the two short axes represent the variability among the measurements by the different operators. The ratio of the short axes to the long axis (b/a and c/a) can indirectly quantify measurement reliability, with smaller ratios indicating higher reliability, as the points are more closely aligned along a straight line. Stroke volume shows higher reliability (b/a =13% and c/a =9%) compared to net flow rate (b/a =26% and c/a =19%).

Intrarater reliability of aqueduct parameters

Table 2 presents the intrarater reliability distribution for the three operators, alongside the mean differences and

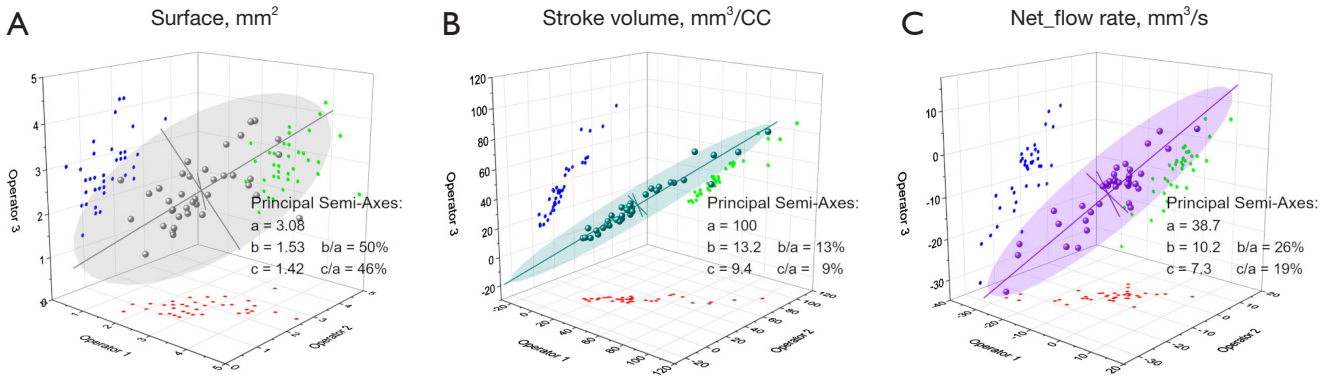

Figure 5 Distribution of operators' measurements. 3D scatter plots display the distribution of three parameters measured by three operators. Gray, cyan, and purple represent (A) surface area (mm^2), (B) stroke volume (mm^3/CC), and (C) net flow rate (mm^3/s), with corresponding 95% confidence ellipsoids. Red, blue, and green 2D scatter points indicate pairwise distributions between operators. CC, cardiac cycle.

Table 2 Intrarater reliability quantification of aqueduct flow parameters measured by operators

Parameters	Surface, mm^2	SV, mm^3/CC	Flow_Ampli., mm^3/s	net_flow, mm^3/s	V_Ampli., mm/s	averV_Ref., mm/s	SD_Ref., mm/s
Op-1							
Mean ± SD	2.8±0.75	39±21	301±127	−9.4±7.4	106±28	−1.0±4.1	19.8±6.6
ICC (1,1)	0.84	0.99	0.97	0.92	0.97	0.99	0.97
Difference (unit)	−0.04	−0.13	−1.83	0.76	0.98	0.06	−0.26
LOA range (unit)	1.71	14.6	131	11.3	27.0	1.22	6.34
Op-2							
Mean	2.0±0.62	31±17	238±105	−7.9±7.0	119±34	−1.1±4.1	20.0±7.0
ICC (1,1)	0.33	0.92	0.85	0.78	0.82	0.99	0.94
Difference	0.32	1.56	17.4	−0.01	−11.4	0.07	−0.58
LOA range	2.61	27.8	218	18.6	68.0	1.78	9.89
Op-3							
Mean	2.8±0.87	37±19	289±117	−10.1±8.9	106±33	−1.0±4.1	20.0±7.0
ICC (1,1)	0.54	0.95	0.91	0.87	0.88	0.97	0.92
Difference	0.21	2.02	13.0	−0.70	−1.30	0.25	−0.59
LOA range	3.25	23.8	188	18.0	64.2	4.22	11.1

Op-1 denotes Operator 1. Op-2 denotes Operator 2. Op-3 denotes Operator 3. 'Mean' represents the average of the two acquisitions. ICC (1,1) quantifies the intrarater reliability of each operator's measurements for each parameter. 'Difference' and 'LOA range' are derived from Bland-Altman analysis, indicating the mean difference and the range of the 95% limits of agreement (LOA = mean ± 1.96 × SD) between the first and second acquisitions, respectively (LOA range = upper LOA − lower LOA). Flow_Ampli. indicates the amplitude of the flow curve, net_flow represents the average value of the mean cardiac cycle flow curve and V_Ampli. represents the amplitude of the mean velocity curve. AverV_Ref. denotes the average velocity within the background reference ROI, while SD_Ref. represents the standard deviation of velocity within the background reference ROI. ICC, intraclass correlation coefficient; SD, standard deviation; SV, stroke volume; CC, cardiac cycle; LOA, limits of agreement.

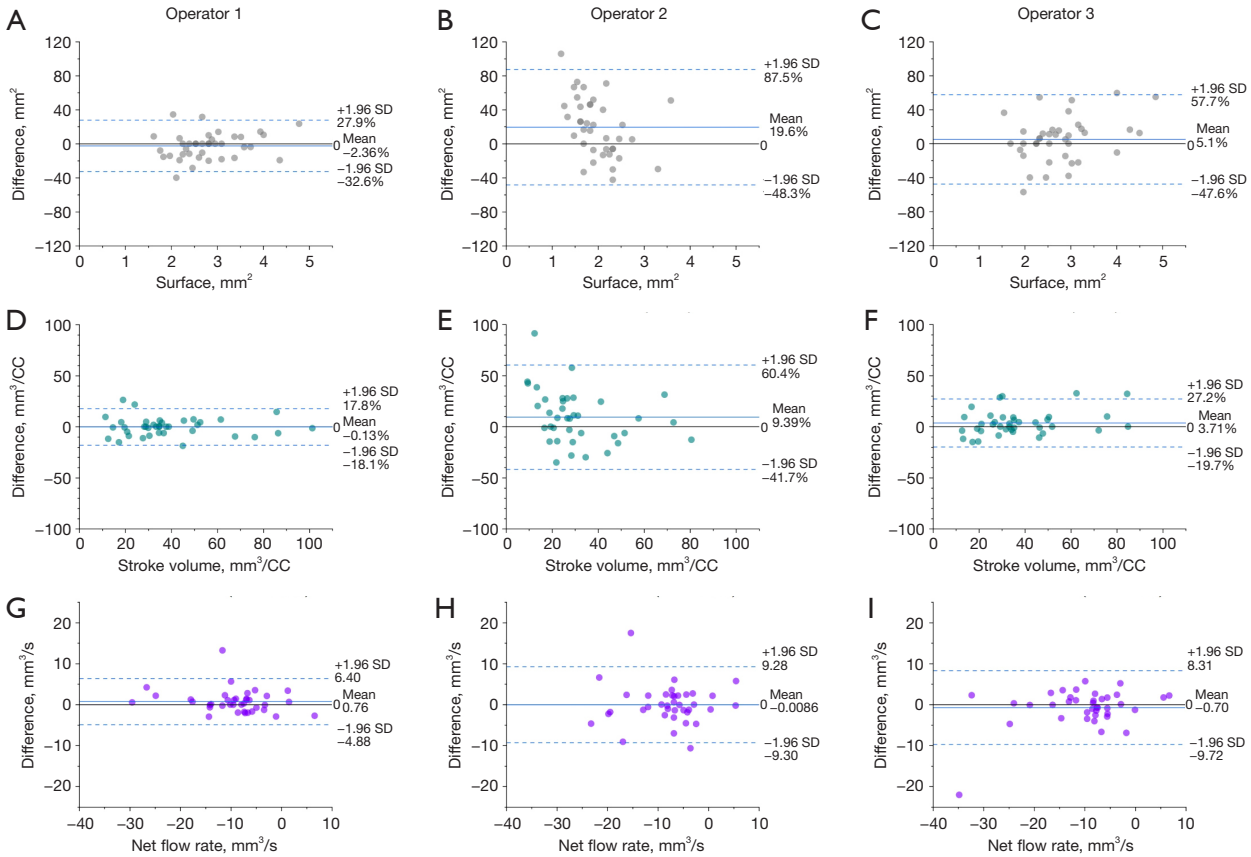

Figure 6 Bland-Altman plots for surface, stroke volume, and net flow rate, based on two measurements across the three operators. The X-axis represents the mean of the two measurements, while the Y-axis shows their differences: percentage differences for surface and stroke volume, and absolute differences for net flow rate. The mean difference and limits of agreement (LOA: mean ± 1.96 × SD) are indicated. CC, cardiac cycle; LOA, limits of agreement, SD, standard deviation.

LOA ranges for each parameter as quantified by the Bland-Altman analysis.

Operator 1 demonstrated relatively higher intrarater reliability. Excluding averV_Ref. and SD_Ref., the surface parameter exhibited the lowest intrarater reliability (ICC =0.84, 0.33, 0.54), followed by net flow (ICC =0.92, 0.78, 0.87), while stroke volume showed the highest reliability (ICC =0.99, 0.92, 0.95).

Figure 6 shows the Bland-Altman plots for surface, stroke volume, and net flow across the three operators. The plots indicate that Operator 1 exhibits higher intrarater reliability. Moreover, stroke volume demonstrates greater intrarater reliability compared to surface.

Effect of gender, VENC, age, and cardiac period

As shown in *Figure 7*, gender, age, and cardiac period did not significantly impact the percentage measurement errors of the various parameters. However, VENC affected the measurement reliability of net flow rate. As VENC increased, the percentage difference in flow rate measurements also increased, while the percentage difference in pixel velocity minimum decreased.

Through *Figure 8A*, VENC significantly increases the variability of the average velocity within the reference region and the noise intensity (i.e., the standard deviation of velocity within the reference region). It also decreases the reliability of net flow rate measurements.

Additionally, the surface area and stroke volume in males are significantly greater than in females, and the net flow rate in the negative direction is also significantly greater in males compared to females (*Figure 8B*). The cardiac period is significantly positively correlated with stroke volume (*Figure 8C*).

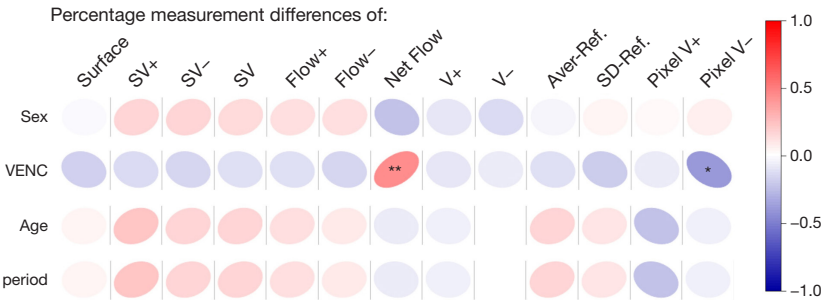

Figure 7 Correlation matrix of gender, VENC, age, and cardiac period with measurement errors of various parameters. The rows represent the four variables (gender, VENC, age, and cardiac period), and the columns represent the percentage differences of each parameter. SV+ denotes the positive direction stroke volume, Flow+ denotes the maximum flow rate in the positive direction, V- denotes the maximum flow velocity in the negative direction, Aver-Ref. denotes the average velocity within the reference ROI, SD denotes the standard deviation of the velocity within the reference ROI, and Pixel V+ represents the maximum flow velocity corresponding to the pixel with the greatest velocity amplitude. Non-parametric correlation test: *, P<0.05; **, P<0.01. ROI, region of interest; SD, standard deviation; VENC, velocity encoding.

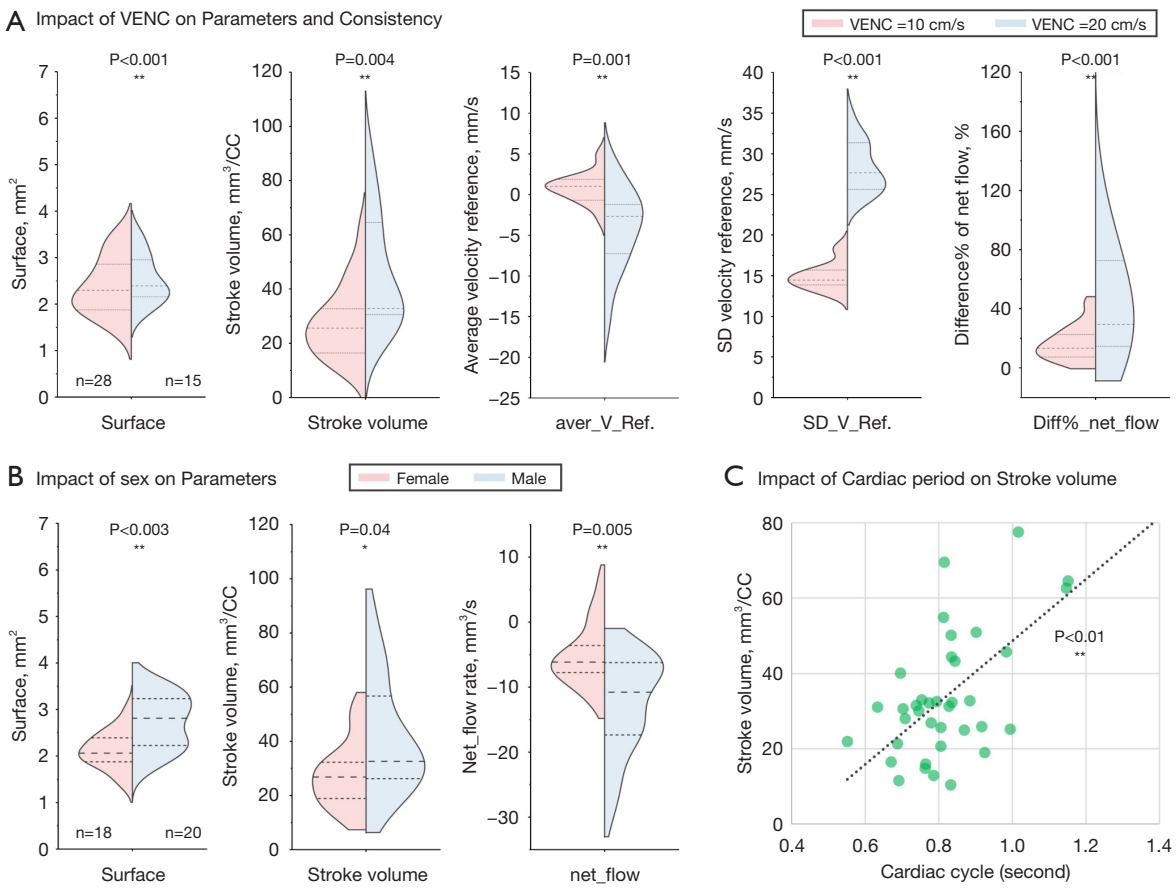

Figure 8 Impact of VENC, sex, and cardiac period on various parameters. (A) Violin plots of parameter distributions at VENC =10 and 20 cm/s. Aver-V-Ref. denotes the mean value of the average velocity within the reference ROI. SD-V-Ref. denotes the mean value of the standard deviation of velocity within the reference ROI. Diff%_Net_flow represents the percentage measurement difference of the net flow rate. (B) Violin plots of parameters for male and female participants. (C) Scatter plot of cardiac period and stroke volume. *, indicates P<0.05; **, indicates P<0.01. CC, cardiac cycle; ROI, region of interest; SD, standard deviation; VENC, velocity encoding.

Discussion

This study quantified the intrarater and interrater reliability of aqueduct flow parameters measured by different operators. Through various analytical methods, we confirmed that most aqueduct flow parameters exhibit high reliability. However, we highlighted some noteworthy parameters, such as surface area and net flow rate, which showed lower reliability. Additionally, we analysed the impact of different parameters on measurement reliability. These results provide valuable references for the clinical application of aqueduct flow data.

Reliability of aqueduct CSF flow parameters: critical importance

The reliability of aqueduct CSF flow parameters is crucial for clinical applications, including diagnosing and monitoring conditions like normal pressure hydrocephalus and aqueduct stenosis. Previous studies have shown that reliable measurements of parameters such as net flow per stroke, flow amplitude, peak mean velocity, and stroke volume are essential for accurate clinical diagnostics (33,34).

Pixel velocity extremes, velocity extremes, and flow rate extremes selection

Among the three parameters, pixel velocity extremes exhibit the highest interrater reliability (*Table 1*), consistent with a previous study (35). Notably, when using a standardized background correction algorithm, the reliability errors primarily stem from the selection of the correct pixel, which may be influenced by aliasing (Table S1). Utilizing an automated pixel selection function could further enhance its quantification reliability. However, it is important to note that pixel velocity extremes contain limited information, making it difficult to derive flow or volume curves.

The velocity extreme represents the average velocity at the time of maximum flow rate, and is more sensitive to Surface parameter compared to Pixel velocity extreme. Previous research has demonstrated that lowering the resolution of PC-MRI also results in a significant underestimation of the velocity extreme. This underestimation is primarily due to an overestimation of the segmentation area (36-38).

However, the impact of an overestimated segmentation area on flow measurements is relatively smaller. Larger pixel sizes reduce the maximum velocity within the ROI, and the additional surrounding areas typically have low flow velocities. As a result, while the mean velocity is significantly reduced, the overestimated area helps maintain the overall accuracy of the flow measurement. As shown in Figures S2-S4, the stroke volume has the highest correlation with flow rate extreme (r=0.90, 0.90, 0.86) and the lowest correlation with average velocity extremes (r=0.61, 0.49, 0.63). It should be noted, though, that spatial resolution only ensures accurate flow rate quantification within certain limits. When spatial resolution decreases beyond a threshold, partial volume effects become dominant, leading to an overestimation of the flow rate.

Given these characteristics, flow rate extremes appear to be more suitable as clinical indicators. The relative insensitivity of flow measurements to segmentation errors makes them a more robust parameter for clinical applications.

Background field correction is necessary

Background field correction is particularly necessary when measuring low-velocity flows, such as quantifying CSF oscillations. Some studies use software algorithms, like velocity standard deviation thresholding, to exclude stationary tissues or empty spaces, which can interfere with background field correction. Therefore, it is advisable to use the original phase-contrast images for CSF flow quantification. In this study, it was observed that the average velocity within the reference region was not constant (*Figure 3E*), indicating the need for dynamic correction of each frame's velocity rather than using a fixed value.

Additionally, background field correction requires a high level of physiological knowledge. The fully automatic algorithm effectively reduces the training time for operators and improves the consistency and accuracy of background field correction (39). After applying background field correction, we observed gender differences in net flow rate (*Figure 8B*).

Surface not suitable for measurement by PC-MRI

In this study, surface area demonstrated the lowest consistency among the measured parameters (*Table 1*), indicating it is not suitable for measurement by PC-MRI. The primary reasons are as follows: Firstly, low VENC phase-contrast images inherently have a low velocity noise ratio, with SD-V-Ref. being 1.5 cm/s at VENC =10 cm/s.

This low velocity noise ratio complicates segmentation, particularly manual segmentation. Secondly, the small size of the aqueduct and the generally low spatial resolution of PC-MRI result in significant percentage differences in measurements.

To accurately quantify the morphological parameters of the aqueduct, it is better to use morphological images with higher spatial resolution. Although the measurement consistency of surface area is low, it does not significantly affect the consistency of flow rate and stroke volume. This is because segmentation differences in surface area typically occur at the boundaries, where the velocity is low.

Net flow exists, but is not suitable for measurement by PC-MRI

This study found that all three operators consistently measured a net flow rate significantly less than zero, indicating a net outflow from the third ventricle to the fourth ventricle. This finding aligns with the current predominant CSF production theories (40,41).

However, it is important to note that the study also revealed that the interrater percentage difference for net flow rate reached 33% (*Table 1*), and its intrarater reliability, as indicated by ICC(1,1), was the lowest among all flow parameters (*Table 2*). Both the ternary scatter plots and the 3D scatter plots demonstrated poor consistency (*Figures 4,5*). The net flow rate is particularly susceptible to external factors, such as increased VENC, which amplifies noise and further reduces consistency (*Figures 7,8A*).

Accurately measuring net flow rate using PC-MRI is challenging for several reasons. Firstly, the net flow rate itself is very small (approximately 5 mm^3/s) and close to the average velocity of the background field (42). Furthermore, CSF oscillations are influenced not only by cardiac activity but also by respiratory cycles, occurring at a frequency of 4–6 seconds (17,20,43-47), and by larger-period brain regulatory oscillations, occurring at a frequency of 10–30 seconds (19). These can significantly affect the net flow rate observed in PC-MRI. While long-term acquisition using real-time phase-contrast sequences might capture the net flow rate more accurately, these applications are currently limited by the duration of data collection.

Therefore, we recommend that the net flow rate be used more as an indicator of trends rather than as a parameter for quantifying individual differences. Special caution should be exercised in clinical applications to account for these limitations.

Limitations and prospects

This study focused on the reliability of both inter-operator measurements and repeated measurements but did not consider the consistency across different software or the reproducibility of parameters with repeated acquisitions in participants. Laganà *et al.* (35) have previously studied the consistency of aqueduct flow parameters across different software, highlighting the need for further research into the reproducibility of parameters with repeated participant acquisitions. Previous studies also have shown that variations in cardiac cycles between acquisitions can significantly affect stroke volume quantification, with a 10% chance of heart rate cycle differences exceeding 10% (20).

Moreover, our study's age distribution was relatively narrow, focusing on participants aged 19–35 years. Therefore, the finding that age does not affect parameter consistency should be interpreted cautiously and is only applicable to this specific age range. Future research should include a broader age range to validate whether these findings hold true across different age groups.

Conclusions

This study assessed the interrater and intrarater reliability of aqueduct CSF flow parameters measured by PC-MRI across different operators in healthy adults. By evaluating key parameters such as net flow per stroke, flow rate extremes, peak mean velocity, and stroke volume, we found that most parameters exhibited good to excellent reliability. However, net flow rate and surface area showed moderate consistency, highlighting the need for careful consideration when using these measures clinically. The impact of VENC, sex, age, and cardiac period on measurement variability was also analysed, revealing that higher VENC can decrease the reliability of net flow rate, and that males exhibited higher surface area, stroke volume, and net flow rate (third to fourth ventricles) compared to females. These findings underscore the importance of validating CSF hydrodynamic parameters for robust clinical application in diagnosing and monitoring neurodegenerative diseases, providing a valuable reference for future research and clinical practices.

Acknowledgments

Thanks to David Chechin from Phillips Industry for scientific support and Héléna Freulet, Garance

Arbeaumont-Trocmé, Marion Vilhem, Lisa Petrieux and Julien Van Gysel (MRI research technicians) for assistance with the acquisition of high-quality images.

Footnote

Reporting Checklist: The authors have completed the GRRAS reporting checklist. Available at https://qims.amegroups.com/article/view/10.21037/qims-24-1589/rc

Funding: This research was funded by the France National Research Agency (reference: Hanuman ANR-18-CE45–0014 and EquipEX Fig. 10-EQPX-0001).

Conflicts of Interest: All authors have completed the ICMJE uniform disclosure form (available at https://qims.amegroups.com/article/view/10.21037/qims-24-1589/coif). All authors report that this study was funded by the France National Research Agency (reference: Hanuman ANR-18-CE45–0014 and EquipEX Fig. 10-EQPX-0001). The authors have no other conflicts of interest to declare.

Ethical Statement: The authors are accountable for all aspects of the work in ensuring that questions related to the accuracy or integrity of any part of the work are appropriately investigated and resolved. This study was conducted in accordance with the Declaration of Helsinki and its subsequent amendments. This study was approved by the local Ethics Review Committee (CPP Nord Ouest II, Amiens, France; reference: PI2019_843_0056). Informed consent was obtained from all individual participants involved in the study.

References

1. Iliff JJ, Wang M, Liao Y, Plogg BA, Peng W, Gundersen GA, Benveniste H, Vates GE, Deane R, Goldman SA, Nagelhus EA, Nedergaard M. A paravascular pathway facilitates CSF flow through the brain parenchyma and the clearance of interstitial solutes, including amyloid β. Sci Transl Med 2012;4:147ra111.
2. Zhou L, Nguyen TD, Chiang GC, Wang XH, Xi K, Hu TW, Tanzi EB, Butler TA, de Leon MJ, Li Y. Parenchymal CSF fraction is a measure of brain glymphatic clearance and positively associated with amyloid beta deposition on PET. Alzheimers Dement 2024;20:2047-57.
3. Cai Y, Zhang Y, Leng S, Ma Y, Jiang Q, Wen Q, Ju S, Hu J. The relationship between inflammation, impaired glymphatic system, and neurodegenerative disorders: A vicious cycle. Neurobiol Dis 2024;192:106426.
4. Zhou L, Butler TA, Wang XH, Xi K, Tanzi EB, Glodzik L, Chiang GC, de Leon MJ, Li Y. Multimodal assessment of brain fluid clearance is associated with amyloid-beta deposition in humans. J Neuroradiol 2024;51:101164.
5. Wen Q, Wang H, Haacke EM, Jiang Q, Hu J. Contribution of Direct Cerebral Vascular Transport in Brain Substance Clearance. Aging Dis 2024;15:584-600.
6. Wright AM, Wu YC, Feng L, Wen Q. Diffusion magnetic resonance imaging of cerebrospinal fluid dynamics: Current techniques and future advancements. NMR Biomed 2024;37:e5162.
7. Karki P, Cogswell P, Murphy M, Ganji S, Graff-Radford J, Alder B, et al. Fluid mechanics based distinct cerebrospinal fluid dynamics signature in normal pressure hydrocephalus. In Toronto (ON), Canada: International Society for Magnetic Resonance in Medicine; 2023.
8. Capel C, Padovani P, Launois PH, Metanbou S, Balédent O, Peltier J. Insights on the Hydrodynamics of Chiari Malformation. J Clin Med 2022;11:5343.
9. Cole S, Liu P, Owashi K, Dougan BD, Matys T, Smielewski P, et al. Implementation of CSF flow dynamic assessment with phase-contrast MRI in the diagnostic process of idiopathic normal pressure hydrocephalus. In: Brain and Spine [Internet]. 2023 [cited 2024 Jul 8]. p. 102294. (Abstracts of the EANS2023; vol. 3). Available online: https://www.sciencedirect.com/science/article/pii/S2772529423005829
10. Yamada S, Ishikawa M, Nozaki K. Exploring mechanisms of ventricular enlargement in idiopathic normal pressure hydrocephalus: a role of cerebrospinal fluid dynamics and motile cilia. Fluids Barriers CNS 2021;18:20.
11. Eide PK, Valnes LM, Lindstrøm EK, Mardal KA, Ringstad G. Direction and magnitude of cerebrospinal fluid flow vary substantially across central nervous system diseases. Fluids Barriers CNS 2021;18:16.

12. Balédent O, Gondry-Jouet C, Meyer ME, De Marco G, Le Gars D, Henry-Feugeas MC, Idy-Peretti I. Relationship between cerebrospinal fluid and blood dynamics in healthy volunteers and patients with communicating hydrocephalus. Invest Radiol 2004;39:45-55.
13. Tawfik AM, Elsorogy L, Abdelghaffar R, Naby AA, Elmenshawi I. Phase-Contrast MRI CSF Flow Measurements for the Diagnosis of Normal-Pressure Hydrocephalus: Observer Agreement of Velocity Versus Volume Parameters. AJR Am J Roentgenol 2017;208:838-43.
14. Tomita Y, Yagi M, Seki F, Komaki Y, Suzuki S, Watanabe K, Matsumoto M, Nakamura M. The significance of cerebrospinal fluid dynamics in adolescent idiopathic scoliosis using time-SLIP MRI. Sci Rep 2024;14:12214.
15. Liu P, Monnier H, Owashi K, Constans JM, Capel C, Balédent O. The Effects of Free Breathing on Cerebral Venous Flow: A Real-Time Phase Contrast MRI Study in Healthy Adults. J Neurosci 2024;44:e0965232023.
16. Liu P, Fall S, Balédent O. Use of real-time phase-contrast MRI to quantify the effect of spontaneous breathing on the cerebral arteries. Neuroimage 2022;258:119361.
17. Burman R, Alperin N. CSF-to-blood toxins clearance is modulated by breathing through cranio-spinal CSF oscillation. J Sleep Res 2024;33:e14029.
18. Wilson MH. Monro-Kellie 2.0: The dynamic vascular and venous pathophysiological components of intracranial pressure. J Cereb Blood Flow Metab 2016;36:1338-50.
19. Wang Y, van Gelderen P, de Zwart JA, Özbay PS, Mandelkow H, Picchioni D, Duyn JH. Cerebrovascular activity is a major factor in the cerebrospinal fluid flow dynamics. Neuroimage 2022;258:119362.
20. Liu P, Owashi K, Monnier H, Metanbou S, Capel C, Balédent O. Validating the accuracy of real-time phase-contrast MRI and quantifying the effects of free breathing on cerebrospinal fluid dynamics. Fluids Barriers CNS 2024;21:25.
21. Maier SE, Hardy CJ, Jolesz FA. Brain and cerebrospinal fluid motion: real-time quantification with M-mode MR imaging. Radiology 1994;193:477-83.
22. Sakakibara Y, Yatsushiro S, Konta N, Horie T, Kuroda K, Matsumae M. Respiratory-driven Cyclic Cerebrospinal Fluid Motion in the Intracranial Cavity on Magnetic Resonance Imaging: Insights into the Pathophysiology of Neurofluid Dysfunction. Neurol Med Chir (Tokyo) 2021;61:711-20.
23. Balédent O, Henry-Feugeas MC, Idy-Peretti I. Cerebrospinal fluid dynamics and relation with blood flow: a magnetic resonance study with semiautomated cerebrospinal fluid segmentation. Invest Radiol 2001;36:368-77.
24. Sincomb S, Moral-Pulido F, Campos O, Martínez-Bazán C, Haughton V, Sánchez AL. An in vitro experimental investigation of oscillatory flow in the cerebral aqueduct. Eur J Mech B Fluids 2024;105:180-91.
25. Liu P, Owashi K, Monnier H, Metanbou S, Capel C, Balédent O. Transmantle pressure under the influence of free breathing: non-invasive quantification of the aqueduct pressure gradient in healthy adults. Fluids Barriers CNS 2025;22:1.
26. Capel C, Owashi K, Metanbou S, Peltier J, Balédent O. Impact of Shunt Placement on CSF Dynamics. Biomedicines 2023;12:20.
27. Stoquart-El Sankari S, Lehmann P, Gondry-Jouet C, Fichten A, Godefroy O, Meyer ME, Baledent O. Phase-contrast MR imaging support for the diagnosis of aqueductal stenosis. AJNR Am J Neuroradiol 2009;30:209-14.
28. Stehling MK, Firth JL, Worthington BS, Guilfoyle DN, Ordidge RJ, Coxon R, Blamire AM, Gibbs P, Bullock P, Mansfield P. Observation of cerebrospinal fluid flow with echo-planar magnetic resonance imaging. Br J Radiol 1991;64:89-97.
29. Pelc NJ, Herfkens RJ, Shimakawa A, Enzmann DR. Phase contrast cine magnetic resonance imaging. Magn Reson Q 1991;7:229-54.
30. Kottner J, Audige L, Brorson S, Donner A, Gajewski BJ, Hróbjartsson A, Roberts C, Shoukri M, Streiner DL. Guidelines for Reporting Reliability and Agreement Studies (GRRAS) were proposed. Int J Nurs Stud 2011;48:661-71.
31. Liu P, Fall S, Baledent O. Flow 2.0 - a flexible, scalable, cross-platform post-processing software for real-time phase contrast sequences. In London, England, UK: ISMRM 2022; 2022. Available online: https://archive.ismrm.org/2022/2772.html
32. Liu P. Acquisition et traitement de l'imagerie par Résonance Magnétique en contraste de phase pour la quantification des écoulements cérébraux du sang et du Liquide Cérébro-Spinal sous influence respiratoire [Internet] [Theses]. Université de Picardie Jules Verne; 2021 [cited 2022 Oct 26]. Available online: https://hal.archives-ouvertes.fr/tel-03749817
33. Luetmer PH, Huston J, Friedman JA, Dixon GR, Petersen RC, Jack CR, McClelland RL, Ebersold MJ. Measurement of cerebrospinal fluid flow at the cerebral aqueduct by use

of phase-contrast magnetic resonance imaging: technique validation and utility in diagnosing idiopathic normal pressure hydrocephalus. Neurosurgery 2002;50:534-43; discussion 543-4.
34. Chen CH, Cheng YC, Huang CY, Chen HC, Chen WH, Chai JW. Accuracy of MRI derived cerebral aqueduct flow parameters in the diagnosis of idiopathic normal pressure hydrocephalus. J Clin Neurosci 2022;105:9-15.
35. Laganà MM, Jakimovski D, Bergsland N, Dwyer MG, Baglio F, Zivadinov R. Measuring Aqueduct of Sylvius Cerebrospinal Fluid Flow in Multiple Sclerosis Using Different Software. Diagnostics (Basel) 2021.
36. Liu P, Fall S, Ahiatsi M, Balédent O. Real-time phase contrast MRI versus conventional phase contrast MRI at different spatial resolutions and velocity encodings. Clin Imaging 2023;94:93-102.
37. Tang C, Blatter DD, Parker DL. Accuracy of phase-contrast flow measurements in the presence of partial-volume effects. J Magn Reson Imaging 1993;3:377-85.
38. Greil G, Geva T, Maier SE, Powell AJ. Effect of acquisition parameters on the accuracy of velocity encoded cine magnetic resonance imaging blood flow measurements. J Magn Reson Imaging 2002;15:47-54.
39. Fischer C, Wetzl J, Schaeffter T, Giese D. Fully automated background phase correction using M-estimate SAmple consensus (MSAC)-Application to 2D and 4D flow. Magn Reson Med 2022;88:2709-17.
40. Cipolla MJ. The Cerebral Circulation. Colloquium Series on Integrated Systems Physiology: From Molecule to Function. Morgan & Claypool 20091;1:1-59.
41. Heyman A, Patterson JL Jr, Duke TW, Battey LL. The cerebral circulation and metabolism in arteriosclerotic and hypertensive cerebrovascular disease; with observations on the effects of inhalation of different concentrations of oxygen. N Engl J Med. 1953 Aug 6;249(6):223-9.
42. Korbecki A, Zimny A, Podgórski P, Sąsiadek M, Bladowska J. Imaging of cerebrospinal fluid flow: fundamentals, techniques, and clinical applications of phase-contrast magnetic resonance imaging. Pol J Radiol 2019;84:e240-50.
43. Chen L, Beckett A, Verma A, Feinberg DA. Dynamics of respiratory and cardiac CSF motion revealed with real-time simultaneous multi-slice EPI velocity phase contrast imaging. Neuroimage 2015;122:281-7.
44. Aktas G, Kollmeier JM, Joseph AA, Merboldt KD, Ludwig HC, Gärtner J, Frahm J, Dreha-Kulaczewski S. Spinal CSF flow in response to forced thoracic and abdominal respiration. Fluids Barriers CNS 2019;16:10.
45. Liu P, Owashi K, Monnier H, Metanbou S, Capel C, Balédent O. Cardiac and respiratory activities induce temporal changes in cerebral blood volume, balanced by a mirror CSF volume displacement in the spinal canal. Neuroimage 2025;305:120988.
46. Gutiérrez-Montes C, Coenen W, Vidorreta M, Sincomb S, Martínez-Bazán C, Sánchez AL, Haughton V. Effect of Normal Breathing on the Movement of CSF in the Spinal Subarachnoid Space. AJNR Am J Neuroradiol 2022;43:1369-74.
47. Dreha-Kulaczewski S, Joseph AA, Merboldt KD, Ludwig HC, Gärtner J, Frahm J. Inspiration is the major regulator of human CSF flow. J Neurosci 2015;35:2485-91.

Cite this article as: Liu P, Attekeble Y, Xie J, Owashi K, Monnier H, Metanbou S, Capel C, Balédent O. Interrater and intrarater reliability of aqueduct CSF flow parameters measured by phase-contrast MRI in healthy adults. Quant Imaging Med Surg 2025;15(7):6399-6413. doi: 10.21037/qims-24-1589

Supplementary

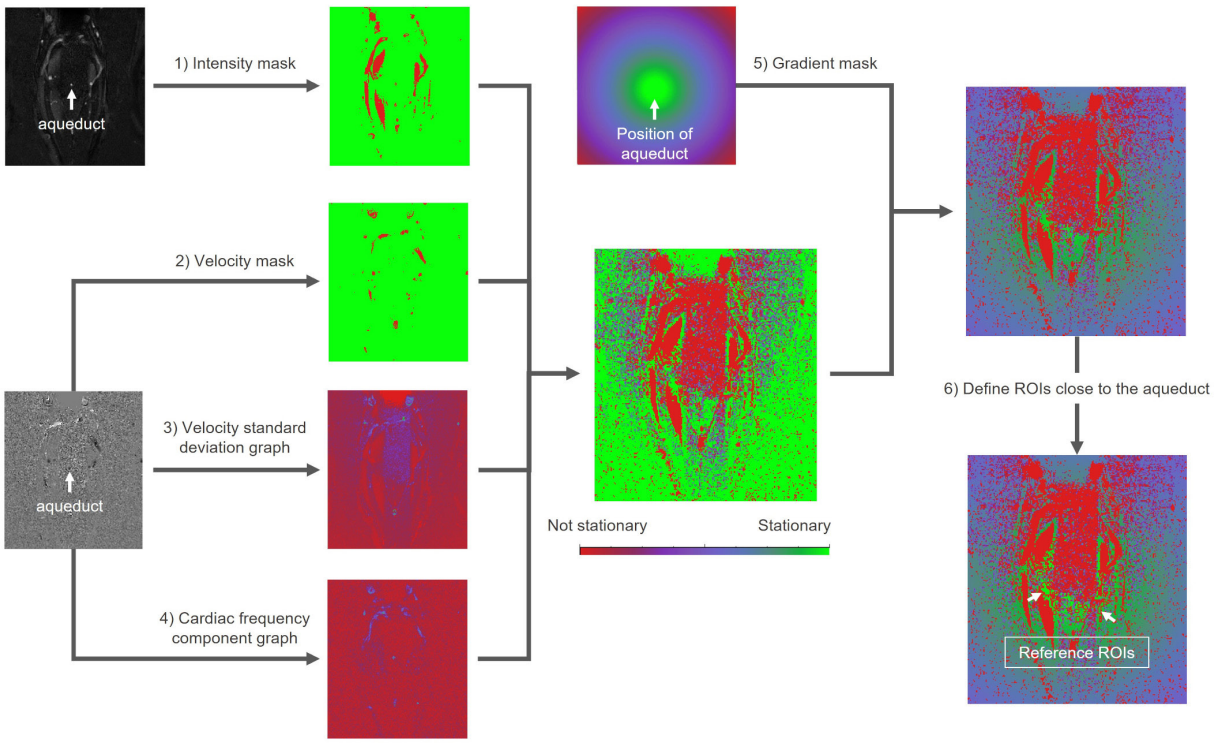

Figure S1 Flowchart for selecting stationary tissues in the background field correction algorithm. CSF, cerebrospinal fluid; ROI, region of interest. The process has the following steps:

1. Subsequent computation is reduced by removing air based on pixel intensity in amplitude images.
2. Analyze the average velocity of each pixel in the phase contrast image and discard blood vessels with absolute average velocities significantly above zero.
3. Exclude areas with high velocity standard deviations, which represent cavities or bone tissue.
4. Perform Fast Fourier Transformation on pixel velocity curves, removing regions with prominent cardiac frequency components, such as the region of CSF.
5. To create the final stationary tissue image, a gradient mask based on the target location is applied to the composite image generated in steps 1–4. The green area indicates stationary tissue near the CSF.
6. Automatically select stationary tissue adjacent to CSF.

https://dx.doi.org/10.21037/qims-24-1589

Table S1 Percentage differences among operators under varying VENC conditions and aliasing status

Parameters	Difference% (n=20), VENC =10 No aliasing	Difference% (n=3), VENC =10 With aliasing	Difference% (n=15), VENC =20 No aliasing
Surface (mm^2)	19.8±10.6	27.6±4.9	17.6±5.9
Stroke volume + (mm^3)	13.3±8.9	18.9±3.4	11.4±5.8
Stroke volume - (mm^3)	11.5±8.0	16.7±3.9	9.6±5.2
Stroke volume (mm^3/CC)	12.3±8.2	17.7±3.7	10.3±4.8
Flow rate Maximum (mm^3/s)	13.5±8.9	19.9±3.9	11.6±5.6
Flow rate minimum (mm^3/s)	12.3±7.1	18.5±3.3	10.1±5.4
Net flow rate (mm^3/s)	16.3±12.2	21.2±6.6	58.4±71.0
Velocity maximum (mm/s)	8.4±5.0	8.9±1.5	7.6±4.1
Velocity minimum (mm/s)	9.8±6.9	10.6±1.7	8.8±4.0
Pixel velocity maximum (mm/s)	4.2±5.9	19.5±13.2	3.5±4.1
Pixel velocity minimum (mm/s)	5.6±4.9	8.1±5.1	2.2±2.6

Percentage differences for each acquisition were calculated using the mean of the three measurements as the reference standard. Data are presented as mean ± standard deviation. VENC, velocity encoding. Under the condition of VENC =10, aliasing significantly increases the percentage differences in pixel velocity extrema (Difference% of Pixel velocity maximum from 4.2% to 19.5%). This is primarily due to aliasing interfering with the operators' ability to accurately select the pixel with the maximum flow velocity. Compared to VENC =10, VENC =20 significantly increases the percentage differences in net flow rate measurements.

https://dx.doi.org/10.21037/qims-24-1589

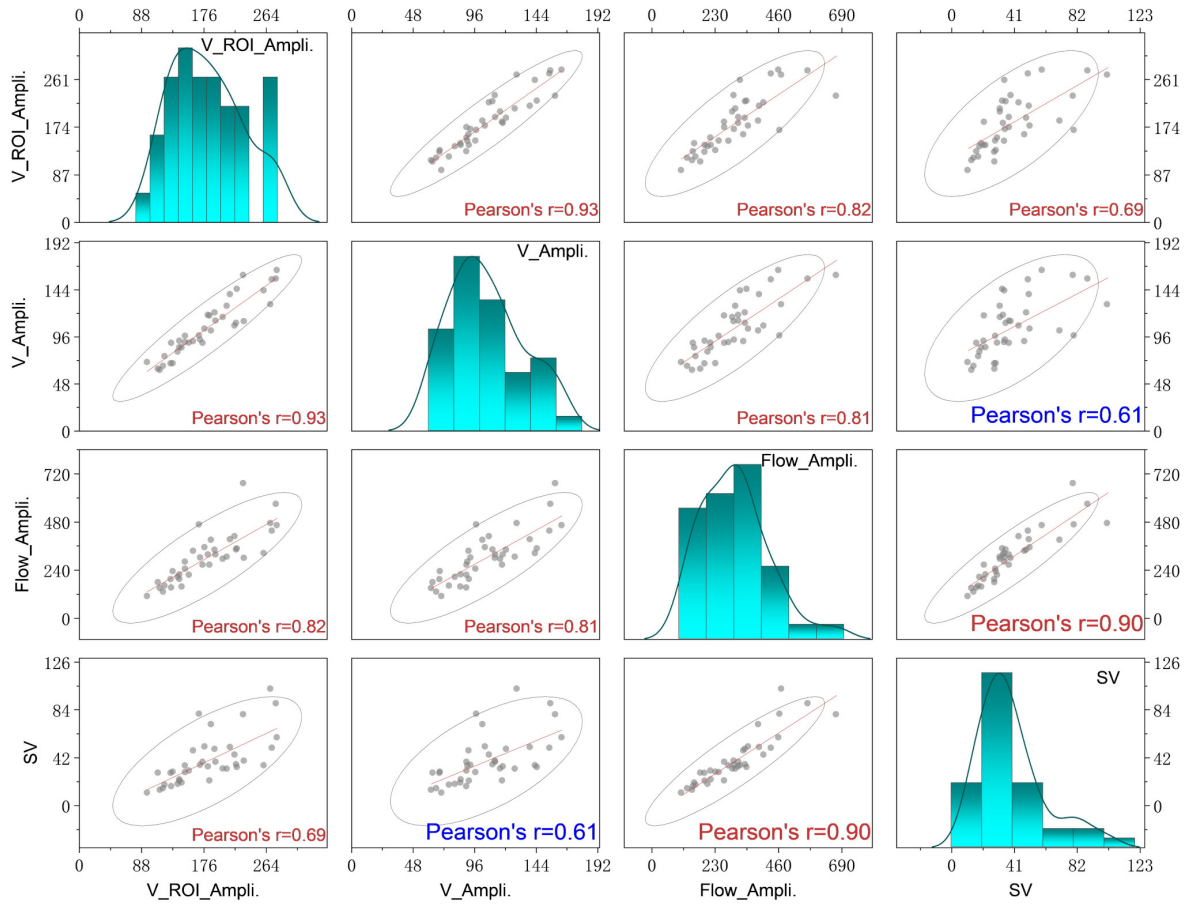

Figure S2 Matrix scatter plot of maximum pixel velocity, average velocity, flow rate, and stroke volume for Operator 1. V_ROI_Ampli. (mm/s) represents the amplitude of the maximum pixel velocity curve within the ROI; V_Ampli. (mm/s) denotes the amplitude of the average velocity curve within the ROI; Flow_Ampli. (mm^3/s) represents the amplitude of the flow curve, calculated as the mean flow rate multiplied by the area of the aqueduct ROI; and SV (mm^3/CC) represents stroke volume, calculated as the average of stroke volumes in both directions. The scatter plots display data distribution, 95% confidence ellipses, linear correlation lines, and Pearson R values, with all P values < 0.01. ROI, region of interest; SV, stroke volume.

https://dx.doi.org/10.21037/qims-24-1589

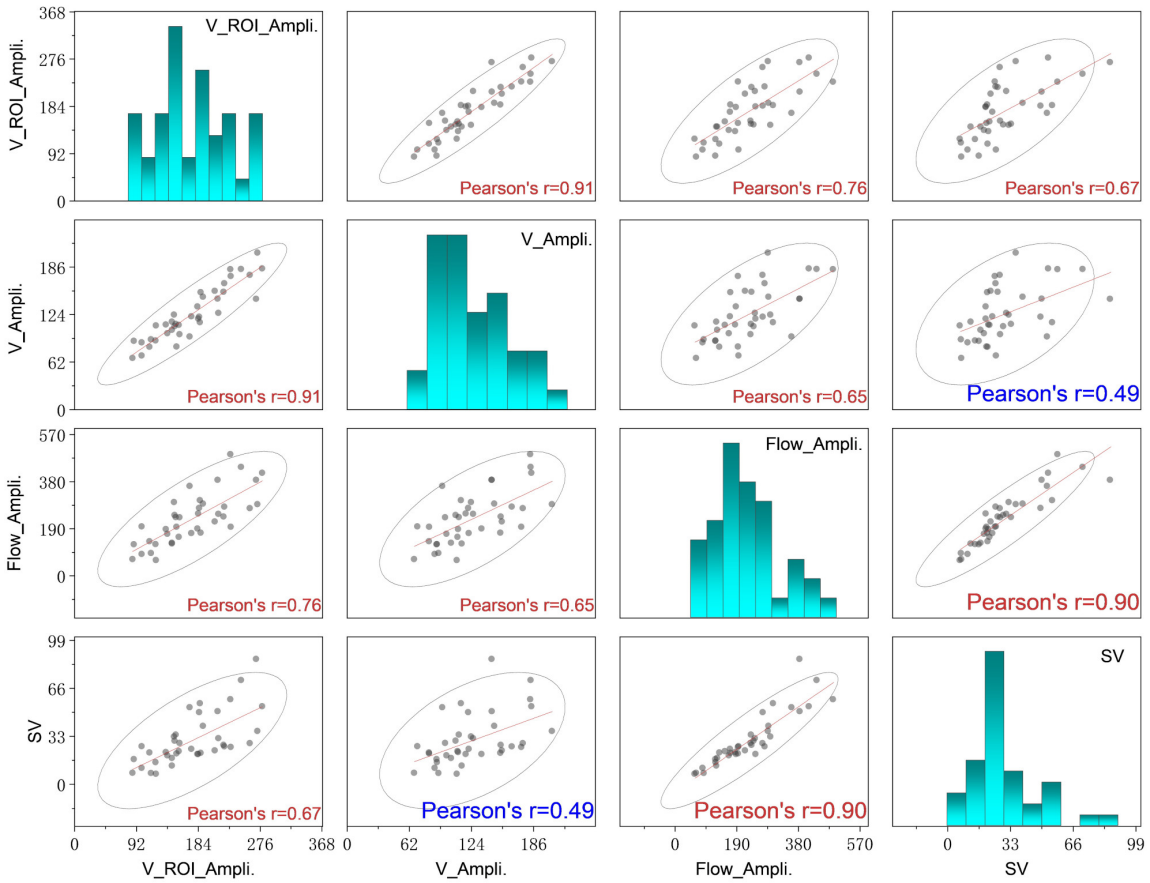

Figure S3 Matrix scatter plot of maximum pixel velocity, average velocity, flow rate, and stroke volume for Operator 2. V_ROI_Ampli. (mm/s) represents the amplitude of the maximum pixel velocity curve within the ROI; V_Ampli. (mm/s) denotes the amplitude of the average velocity curve within the ROI; Flow_Ampli. (mm^3/s) represents the amplitude of the flow curve, calculated as the mean flow rate multiplied by the area of the aqueduct ROI; and SV (mm^3/CC) represents stroke volume, calculated as the average of stroke volumes in both directions. The scatter plots display data distribution, 95% confidence ellipses, linear correlation lines, and Pearson R values, with all P values <0.01. ROI, region of interest; SV, stroke volume.

https://dx.doi.org/10.21037/qims-24-1589

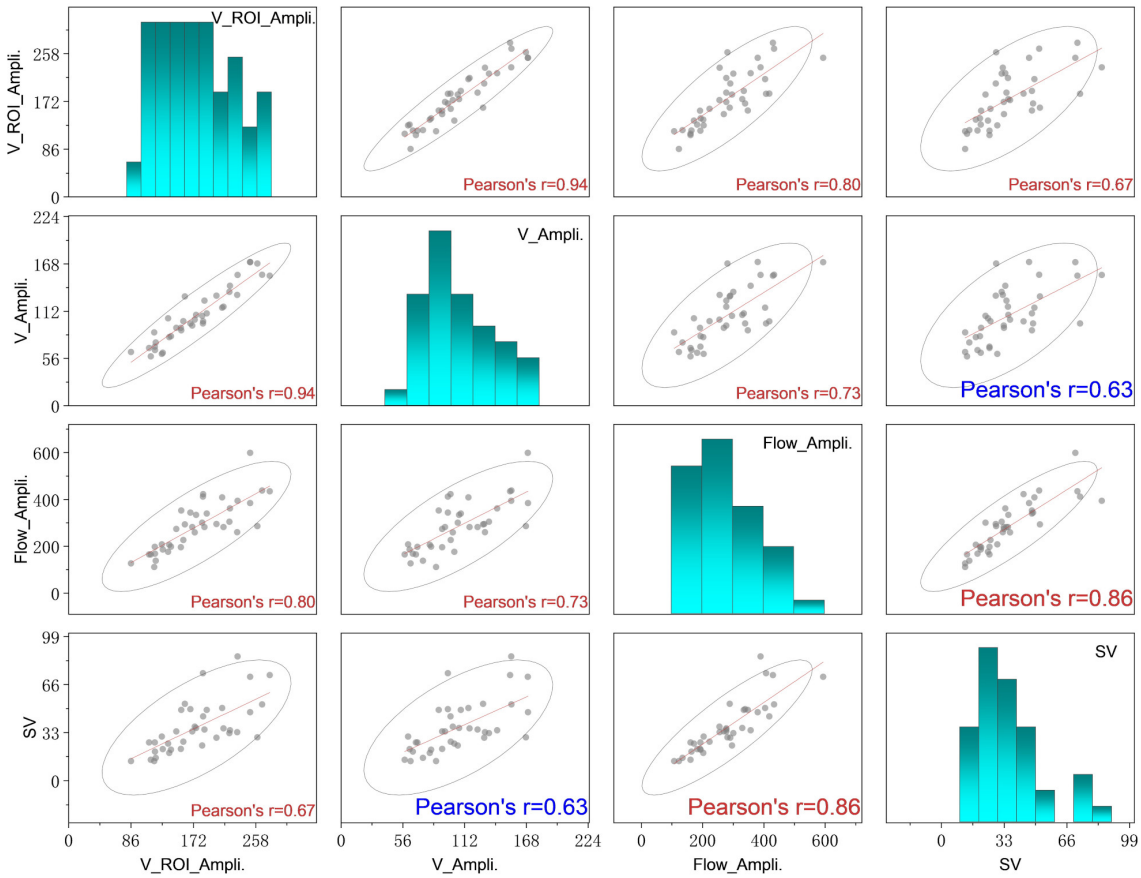

Figure S4 Matrix scatter plot of maximum pixel velocity, average velocity, flow rate, and stroke volume for Operator 3. V_ROI_Ampli. (mm/s) represents the amplitude of the maximum pixel velocity curve within the ROI; V_Ampli. (mm/s) denotes the amplitude of the average velocity curve within the ROI; Flow_Ampli. (mm^3/s) represents the amplitude of the flow curve, calculated as the mean flow rate multiplied by the area of the aqueduct ROI; and SV (mm^3/CC) represents stroke volume, calculated as the average of stroke volumes in both directions. The scatter plots display data distribution, 95% confidence ellipses, linear correlation lines, and Pearson R values, with all P values <0.01. ROI, region of interest; SV, stroke volume.

https://dx.doi.org/10.21037/qims-24-1589